

Single-Slice-to-3D Reconstruction in Medical Imaging and Natural Objects: A Comparative Benchmark with SAM 3D

Yan Luo[†], Advaith Ravishankar[†], Serena Liu[†], Yutong Yang,
Mengyu Wang^{*}

Harvard AI and Robotics Lab, Harvard University.

^{*}Corresponding author(s). E-mail(s): mengyu_wang@meei.harvard.edu;

Contributing authors: yluo16@meei.harvard.edu;

aravishankar@g.harvard.edu; serenaliu1@college.harvard.edu;

yutongyang@hsph.harvard.edu;

[†]These authors contributed equally to this work.

Abstract

A 3D understanding of anatomy is central to diagnosis and treatment planning, yet volumetric imaging remains costly with long wait times. Image-to-3D foundations models can solve this issue by reconstructing 3D data from 2D modalites. Current foundation models are trained on natural image distributions to reconstruct naturalistic objects from a single image by leveraging geometric priors across pixels. However, it is unclear whether these learned geometric priors transfer to medical data. In this study, we present a controlled zero-shot benchmark of single slice medical image-to-3D reconstruction across five state-of-the-art image-to-3D models: SAM3D, Hunyuan3D-2.1, Direct3D, Hi3DGen, and TripoSG. These are evaluated across six medical datasets spanning anatomical and pathological structures and two natrual datasets, using voxel based metrics and point cloud distance metrics. Across medical datasets, voxel based overlap remains moderate for all models, consistent with a depth reconstruction failure mode when inferring volume from a single slice. In contrast, global distance metrics show more separation between methods: SAM3D achieves the strongest overall topological similarity to ground truth medical 3D data, while alternative models are more prone to over-simplification of reconstruction. Our results quantify the limits of single-slice medical reconstruction and highlight depth ambiguity caused by the planar nature of 2D medical data, motivating multi-view image-to-3D reconstruction to enable reliable medical 3D inference.

1 Introduction

A three-dimensional understanding of anatomical and pathological structures is fundamental to clinical practice, enabling accurate assessment of organ morphology. In cardiovascular imaging, 2D echocardiography can underestimate ventricular volume, potentially delaying diagnosis over its 3D counterpart [1]. In breast imaging, the three-dimensional view provided by digital breast tomosynthesis (DBT) can reveal abnormalities otherwise masked by overlapping tissues in 2D mammography [2, 3]. Similarly, chest computed tomography (CT) allows visualization of nodules and lesions that may be missed on 2D radiographs [4]. Despite the benefits of 3D imaging over 2D, 3D imaging techniques remain costly and have long wait times to obtain scans [5, 6].

To mitigate these limitations, image-to-3D reconstruction methods aim to infer 3D structure from 2D data, reducing acquisition time with easier available machinery. Initial generative approaches like X2CT-GAN [7] demonstrated limited-view 3D reconstruction with radiographs. This was later improved upon with single-input methods using diffusion with xdiffusion [8] generating a MRI volume from a single cross-sectional slice. However, these techniques were limited as they are either machine modality specific, or require multiple inputs. This motivates newer approaches that explicitly recover geometry and texture from a single 2D image generalizable to any measurement modality.

The latest image-to-3D foundation models are trained on natural-image distributions with Hunyuan3D-2.1 [9], Direct3D [10], TripoSG [11] and Hi3DGen [12] showing strong reconstruction of naturalistic objects. Among these, SAM3D [13] outperforms alternatives on surface recovery, and object reconstruction [13]. Yet it remains unclear whether the geometric priors learned from natural data transfer to anatomically structured medical domains. Therefore, to address this gap, we benchmark the zero-shot performance of SAM3D on medical datasets. We evaluate reconstruction quality using local and global shape metrics, and compare against Direct3D, Hunyuan3D-2.1, TripoSG and Hi3DGen. Our goal is not to fine-tune models for peak performance, but to measure reconstruction generalization and identify failure modes that are specific to medical anatomy.

2 Method

2.1 Experimental Design

Image-to-3D Pipeline: Figure 1 outlines the pipeline to generate 3D voxelized representations of anatomical structures as point clouds for SAM3D, Hunyuan3D, Direct3D, Hi3DGen and TripoSG. For each dataset, we select a plane (coronal or axial) and process the .nii files to get a 2D image, 2D binary mask, and 3D point cloud. We apply the binary mask to the 2D image to extract a masked 2D image which functions as

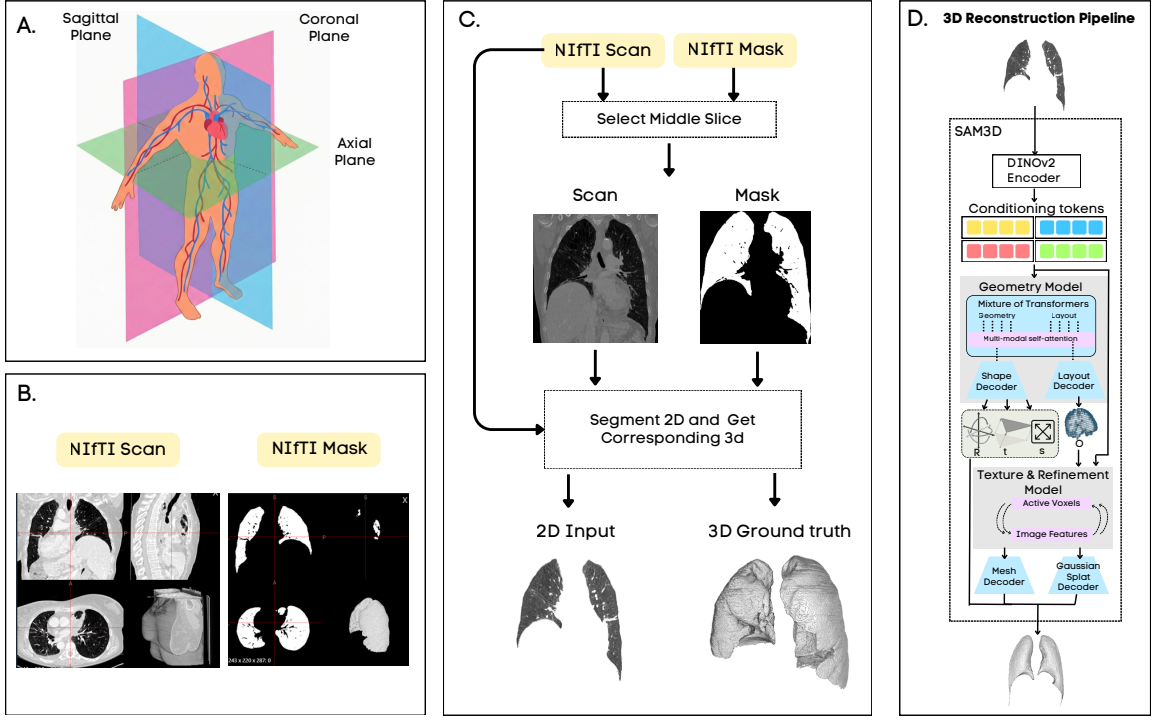


Fig. 1: Zero-shot single-slice medical image-to-3D pipeline. A NIfTI scan and NIfTI segmentation mask are preprocessed to generate a single masked 2D image and a ground truth 3D point cloud. The 2D masked input is passed through SAM3D to get a reconstructed 3D point cloud. We evaluate the reconstruction against the extracted 3D ground truth using the metrics in 2.3.

our input slice. The input slice is passed to the model, which reconstructs the corresponding 3D structure as a point cloud. We then compare the reconstruction against the ground-truth point cloud using the metrics defined in Section 2.3.

2.2 Dataset

Datasets: The information of each dataset is summarized in table 1. We evaluate on a diverse anatomical dataset to show SAM3D’s reconstruction generalization across medical data. Each dataset is in the form of NIfTI (.nii) files which are a stack of 2D slices. In addition, we evaluate on two natural datasets to showcase 3D reconstruction from 2D images with natural geometric priors.

Anatomical and Pathological: For analyzing generalization, we evaluate on both anatomical and pathological structures. Anatomical refers to reconstructing the whole organ from the scan and pathological refers to a subsection of an organ, in this case

Dataset	Type	Modality	Structures Present	Samples
AeroPath [14]	Anatomical	CT	Lungs, Airways	54
BTCV [15]	Anatomical	CT	Spleen, Kidneys, Gall Bladder, Esophagus, liver heart, pancreas, adrenal gland	388
Duke Cspine [16]	Anatomical	MRI	Spinal Cord	2510
MSD Lung [17]	Pathological	CT	Lungs	63
MSD Brain [17]	Pathological	MRI	Brain	1440
MSD Liver [17]	Pathological	CT	Liver	249
Animals3D [18]	Natural	Camera	40 Mammal Species	3379
GSO [19]	Natural	Camera	Common Household Items	1030

Table 1: Datasets used in this study covering anatomical and pathological structures through CT and MRI as well as natural objects and animals. For medical datasets, samples represents number of unique 3D reconstructions for a given plane. As both frontal and axial view are evaluated, the total number of samples computed is doubled.

tumors.

Medical Data Preprocessing: Each instance in our medical datasets contains two NIFTI files: a volumetric scan and its corresponding segmentation mask (as seen Figure 1 part B). The scan stores a 3D anatomical structure as a stack of 2D slices along three orthogonal planes (sagittal, coronal and axial). To construct our ground-truth 3D representation, we extract surface points from the 3D binary mask using morphological erosion: we compute the boundary voxels as the set difference between the original mask and its eroded version, then scale the resulting coordinates by the voxel spacing to obtain a point cloud in physical units.

For the 2D components, we select the midpoint slice along the chosen anatomical plane and extract both the corresponding image and the binary segmentation mask at that slice index. We then apply the mask on the image to get our 2D input slice. This yields our ground-truth data a masked 2D image $I \in \mathbb{R}^{H \times W}$, and a 3D point cloud $P \in \mathbb{R}^{N \times 3}$ representing the surface geometry of the segmented structure. The pipeline is shown visually in Figure 1 part C.

Plane Selection: As seen in Figure 1 part A, the NIFTI files have three planes: sagittal, coronal and axial. We focus on only the coronal and axial planes, as they most consistently provide informative cross-sections of the target anatomy while reducing redundancy and variability from sagittal views.

2.3 Evaluation

Model Comparisons: We benchmark SAM3D against four state-of-the-art diffusion-based image-to-3D generators for reconstruction capabilities. (1) Hunyuan3D-2.1 [9] is a large-scale image-conditioned 3D pipeline that combines a diffusion transformer for shape generation with a diffusion-based texture module to generate reconstructions. (2) Direct3D [10] is a 3D-native latent diffusion transformer that generates 3D

assets directly in a compact 3D latent space, (3) Hi3DGen [12] targets fine geometry generation via an intermediate normal-bridging representation, and (4) TripoSG [11] that uses large-scale rectified-flow (diffusion-style) generative modeling to synthesize high-fidelity 3D shapes with strong geometric fidelity. These approaches provide complementary baseline that span the dominant diffusion based 3D reconstruction approaches, enabling comparison of reconstruction quality.

Metrics: We evaluate the performance of SAM3D, Hunyuan3D-2.1, Direct3D, Hi3DGen and TripoSG on each dataset using five metrics to benchmark the efficacy of our 3D reconstructions. Following each model’s inference protocol for general 3D shape reconstruction, we first normalize both the predicted and ground-truth point clouds to a unit cube in the range $[-1, 1]$ by centering each point cloud at its centroid and scaling by the maximum absolute coordinate. We then apply Iterative Closest Point (ICP) registration to align the predicted point cloud to the ground truth, minimizing pose discrepancies that arise from arbitrary output orientations.

After alignment, we compute the following metrics: (1) **F-score@0.01**, which measures point-cloud surface accuracy and coverage under a 0.01 distance threshold via the harmonic mean of precision and recall; (2) **Voxel-IoU**, which captures coarse volumetric agreement by voxelizing both shapes on a 64^3 grid and computing intersection-over-union; (3) **Chamfer Distance (CD)**, which quantifies local geometric deviation through bidirectional nearest-neighbor distances; and (4) **Earth Mover’s Distance (EMD)**, which measures global structural mismatch via minimum-cost transport between point sets. Additionally, we report (5) **Voxel-Dice**, which is similar to Voxel-IoU but more sensitive to small structures. Together, these metrics cover both local voxel-level and global shape-level comparisons, providing a holistic evaluation of reconstruction quality.

3 Results

Figure 2 and figure 3 summarize the zero-shot 2D single slice to 3D reconstruction performance across our six medical datasets on the coronal and axial planes. We report mean \pm standard deviation over instances as error bars. A higher value is indicative for strong performance for F-score@0.01, Voxel-IoU, and Voxel-Dice, while lower values are better for Chamfer Distance (CD) and Earth Mover’s Distance (EMD). All results in a tabular format can be found in appendix section A.

Voxel Metric Performance: all models exhibited modest to poor performance across these voxel-based metrics, with F1 scores ranging from 0.010 to 0.096, Voxel IoU from 0.013 to 0.157, and Voxel Dice from 0.025 to 0.260 across datasets. This poor performance is because single 2D coronal and axial slices lack geometric cues necessary for accurate depth estimation. Without this information, reconstruction models struggle to recreate an accurate 3D geometry from local, point-based computations.

Distance Metric Performance: In all benchmarked datasets, SAM3D achieved the

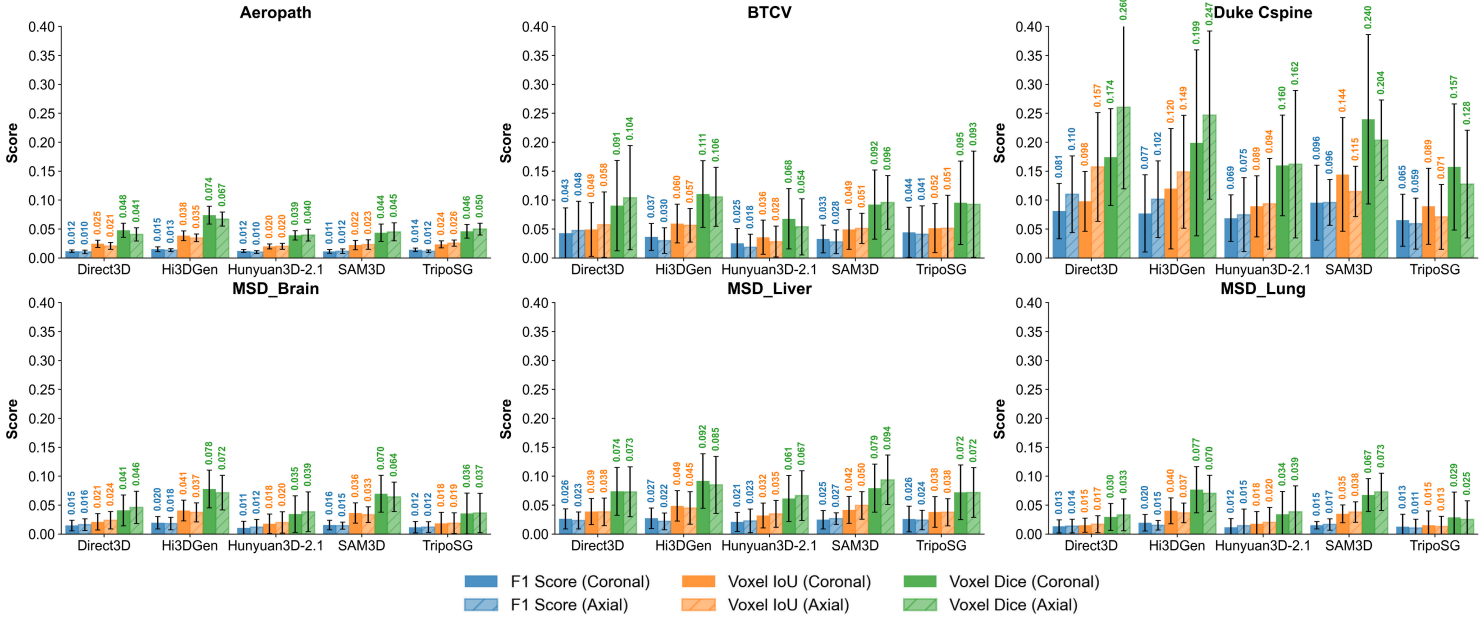


Fig. 2: Voxel-based reconstruction quality metrics across medical datasets. F1 Score, Voxel IoU, and Voxel Dice values evaluated on coronal and axial slice reconstructions for five 3D generation models (Direct3D, Hi3DGen, Hunyuan3D-2.1, SAM3D, TripoSG) across six medical imaging datasets (Aeropath, BTCV, Duke Cspine, MSD_Brain, MSD_Liver, MSD_Lung). Solid bars represent coronal slice metrics; hatched bars represent axial slice metrics. Error bars indicate standard deviation.

lowest, or close to the lowest CD and EMD scores, demonstrating a superior global geometric reconstruction quality. Hi3DGen also showed high performance, but it also had higher variance, particularly on the Duke Cspine dataset where its standard deviation is much larger than SAM3D. This shows that despite all models struggling to estimate local depths, SAM3D better preserves the global shape consistency and the overall point cloud distribution compared to other models.

Medical Qualitative Reconstruction: Figure 5 compares coronal view reconstructions on a sample from AeroPath (lung) and BTCV (liver). From the frontal perspective, 4 out of 5 models (TripoSG fails) are able to reconstruct the silhouette,

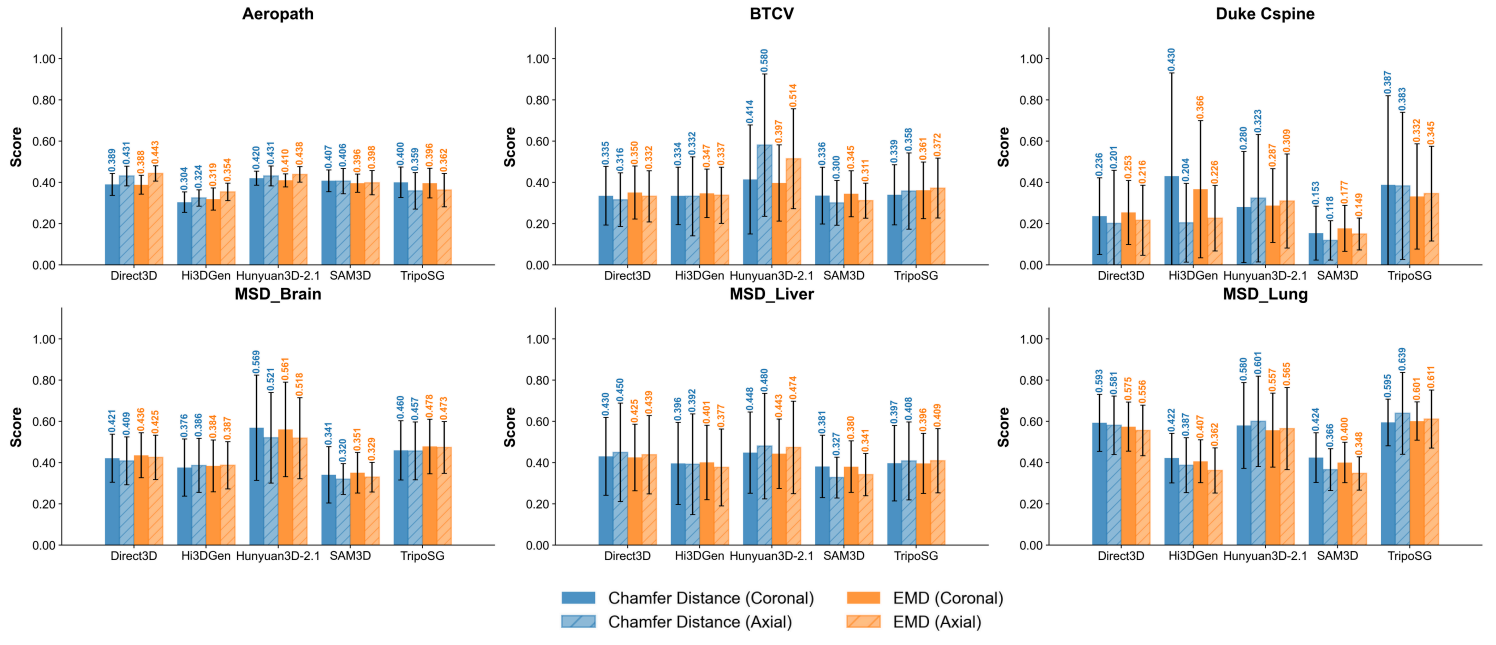


Fig. 3: Point cloud distance metrics across medical datasets. Chamfer Distance and Earth Mover’s Distance (EMD) evaluated on coronal and axial slice reconstructions for five 3D generation models (Direct3D, Hi3DGen, Hunyuan3D-2.1, SAM3D, TripoSG) across six medical imaging datasets (Aeropath, BTCV, Duke Cspine, MSD_Brain, MSD_Liver, MSD_Lung). Solid bars represent coronal slice metrics; hatched bars represent axial slice metrics. Lower values indicate better reconstruction quality. Error bars indicate standard deviation.

but differ in surface regularity. SAM3D most closely matches the ground truth lung silhouette, while Hunyuan3D, and Direct3D capture the overall outline but appear over-smoothed in terms of texture. Hi3DGen exhibits noticeably noisier/rougher geometry, and TripoSG shows stronger structural distortions. On BTCV, the frontal perspective of the liver reconstructions are less stable: Hunyuan3D/Direct3D produce smooth simple shapes, Hi3DGen yields an elongated but mismatched geometry, and TripoSG appears fragmented.

In the depth view, a dominant failure mode across methods is depth reconstruction, where reconstructions become nearly planar, indicating weak recovery of volume from a single 2D slice. This failure is seen in both AeroPath and BTCV, explaining weak

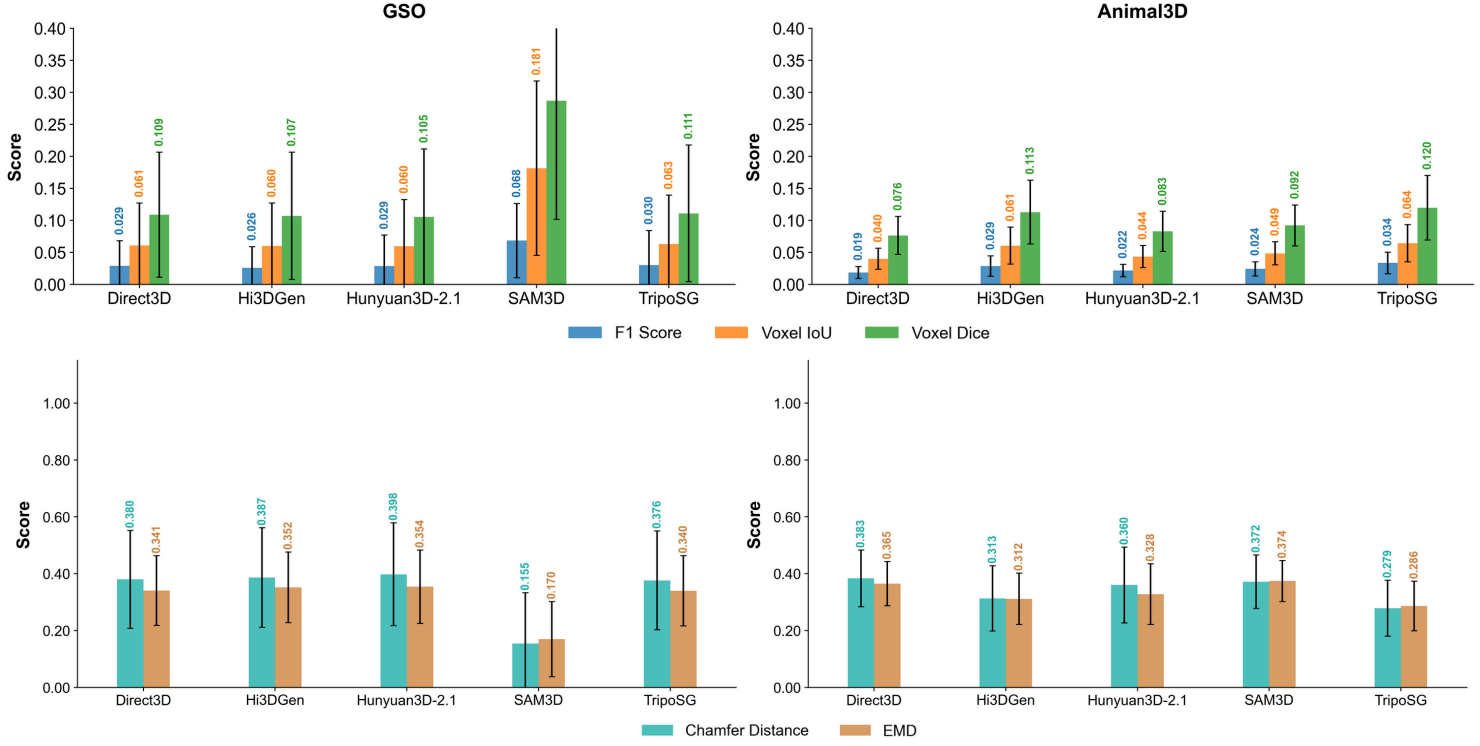


Fig. 4: Voxel and distance-based reconstruction quality metrics across natural datasets. F1 Score, Voxel IoU, Voxel Dice, Chamfer Distance, and EMD values evaluated for five 3D generation models (Direct3D, Hi3DGen, Hunyuan3D-2.1, SAM3D, TripoSG) across two natural datasets (Google Scanned Objects and Animal3D).

performance in terms of voxel scores as depth prediction is weak.

Natural Qualitative Reconstruction: Figure 6 showcases the reconstruction of natural data across all models. All models showcase strong qualitative reconstruction of singular natural objects, with all reconstructions of shoes matching the ground truth. For multiple objects in the scene, however, Hunyuan3D-2.1, Hi3DGen, and Direct3D captures all the objects whereas the TripoSG misses one object and SAM3D misses all but one. This poor performance in multi-object reconstruction is because SAM3D is trained on SA-3DAO scenes that only contain one object reconstruction as the goal. For animals, Hunyuan3D-2.1 and Direct3D struggle to isolate the objects as they exhibit foreground-background entanglement (parts of the ground

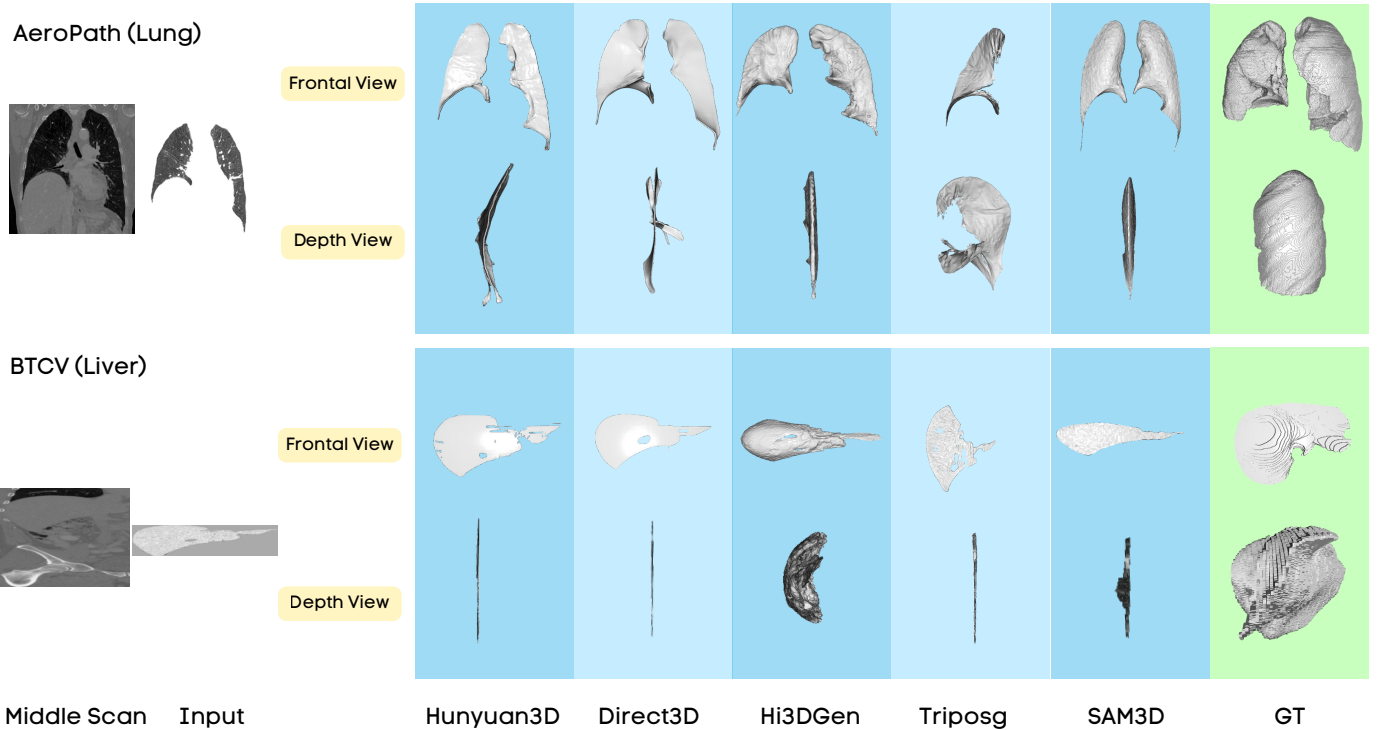


Fig. 5: Coronal view qualitative reconstruction on AeroPath and BTCV from SAM3D

plane/background are fused into the animal mesh), indicating weak object isolation under natural scenes. Both Hi3DGen and TripoSG construct objects well with textures, however, they have additional artifacts associated with the masked image (man on top of the horse is visible). SAM3D achieves the best qualitative reconstruction on the animals, accurately capturing posture and fidelity. Overall, for single object reconstruction, SAM3D qualitatively reconstructs objects reliably.

Coronal vs Axial Plane Qualitative Performance: The coronal based reconstruction partially preserves the silhouette of the lesion region suggested, but loses geometric fidelity as the shape becomes largely sheet-like and regularized (the holes in the tumor become clean circles rather than being a natural structure). Similarly, the axial based reconstruction also yields smooth geometry, but collapses the complex, irregular tumor morphology into an over-regularized shape. Relative to the ground-truth tumor point cloud/mesh (right), both reconstructions fail to recover the highly non-convex, fine-scale boundary irregularities that characterize pathological anatomy.

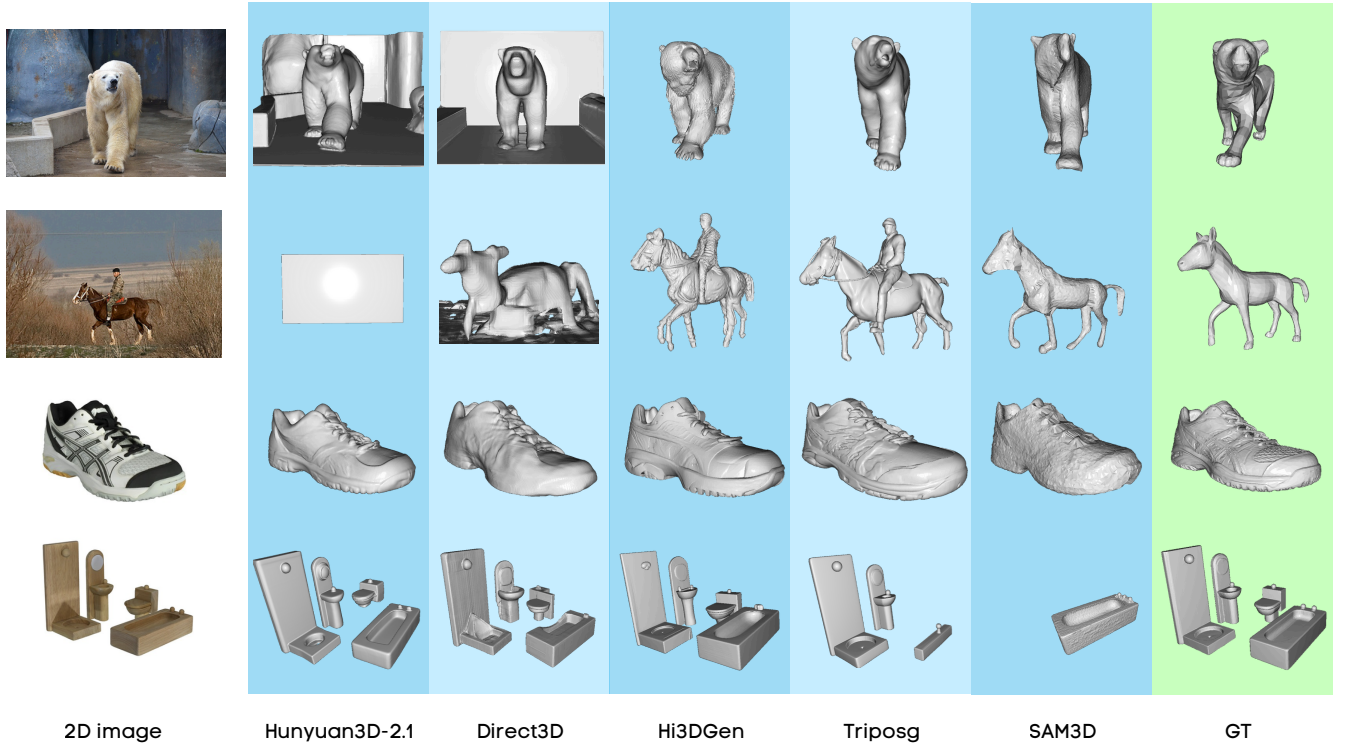


Fig. 6: Natural dataset reconstruction quality across all models

4 Discussion

Why Is Depth Reconstruction Poor?: A dominant failure mode across datasets is depth reconstruction failure: reconstructions become nearly planar (a thin sheet or line in the depth view), indicating that the model is not confidently inferring volume from a single slice. This is because of a priors problem. Image-to-3D generators trained on natural objects implicitly exploit strong geometric cues from shading/texture gradients, occlusion boundaries and spatial depth cues relative to other objects. Medical scans provide none of these cues as slices are often grayscale with limited texture, and relative object depth cues (all objects lie on the same plane). As a result, depth information is lost and 3D depth reconstruction is weak.

Why Is Local Voxel Performance Weak?: As depth predictions are weak, even though silhouette prediction is qualitatively strong as seen in figure 5 and figure 7, the lack of depth predictions leads to unpaired voxels, impairing model performance.

Anatomical and Pathological Structure Performance: Across the anatomical (AeroPath, BTCV, Duke C-spine) and pathological datasets (MSD Lung, MSD

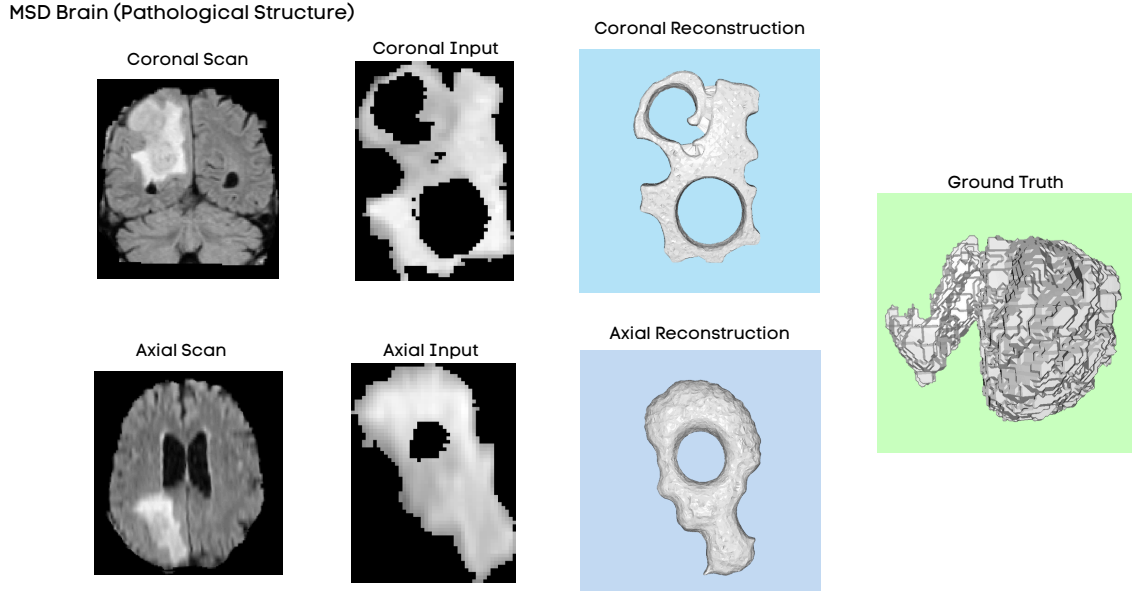


Fig. 7: Comparisons between coronal and axial reconstruction by SAM3D of tumor in MSD Brain

Liver, MSD Brain), voxel-based scores in figure 2 remain modest, highlighting that zero-shot single-slice reconstruction is challenging for medical data.

Natural Object Reconstruction Structure Performance: In contrast, reconstruction performance for the natural object datasets (GSO and Animal3D) is stronger across all models. This can be attributed to the fact that the 3D reconstruction models are primarily trained using natural object data. By generating objects that are more similar in distribution to what they were trained on, the models operate within their learned prior. Additionally, natural images from GSO and Animal3D contain stronger pixel-space geometrical information. Unlike the planar grayscale slices in medical scans, natural images contain depth cues and spatial relationships that allow models to better infer 3D structures from a single view.

Overall Zero-shot image-to-3D Performance using Single Slice: Voxel based local performance is low/poor across all models due to the depth reconstruction failure. On the other had, SAM3D outperforms all other baselines in terms of global distance metrics as seen in figure 3. This is because of the better texture and depth reconstruction of SAM3D as seen in the qualitative reconstructions in figure 5. Hence, SAM3D is the best suited state-of-the-art for Zero-shot image-to-3D performance using single slice medical data.

However, as medical scans lack geometric depth cues with all objects lying on the same depth plane, single slice is ill-posed to reconstruct 3D reconstructions well. To achieve, stronger performance of image-to-3D with medical data, a multi-view reconstruction with aggregation of 3D reconstructions acts as strong formulation to overcome the lack of geometric cues in the data, allowing the foundation models trained to learn geometric priors to achieve Zero-Shot 3D reconstruction.

5 Conclusion

In this work, we benchmarked zero-shot single-slice medical image-to-3D reconstruction using SAM3D and four representative diffusion-based image-to-3D baselines (Hunyuan3D-2.1, Direct3D, Hi3DGen, and TripoSG). Using six medical datasets spanning anatomical and pathological structures (both CT and MRI modalities), we constructed paired masked 2D inputs and 3D surface point-cloud ground truth from NIfTI scan and mask data, and evaluated reconstructions with voxel overlap and point cloud distance metrics.

Across both datasets and models, voxel-based metrics (F-score@0.01, Voxel-IoU, and Voxel-Dice) remained modest, indicating weak volumetric agreement under a single view setting. Qualitative analysis explains that a dominant failure mode is depth reconstruction failure, where reconstructions become planar, despite recovering a reasonable 2D silhouette.

Despite low voxel based performance, global distance metrics (Chamfer Distance and EMD) provide separation among methods in terms of performance. Overall, SAM3D achieves the best geometric similarity to ground truth and the strongest performance on CD and EMD across datasets, suggesting that its learned geometric priors transfer better than competing baselines in a zero-shot regime. However, the lack of depth cues in medical scans indicate that reliable medical 3D reconstruction from a single slice requires constraints such as multi view aggregation across planes.

Appendix A Benchmark Performance Table

Dataset	Model	F-score@0.01	Voxel-IoU	Voxel-Dice	CD	EMD
AeroPath	Hunyuan3D-2.1	0.0112 \pm 0.0027	0.0201 \pm 0.0047	0.0394 \pm 0.0091	0.4256 \pm 0.0418	0.4239 \pm 0.0374
	Direct3D	0.0104 \pm 0.0024	0.0207 \pm 0.0055	0.0406 \pm 0.0105	0.4367 \pm 0.0499	0.4453 \pm 0.0405
	Hi3DGen	0.0143 \pm 0.0035	0.0366 \pm 0.0076	0.0706 \pm 0.0141	0.3137 \pm 0.0460	0.3362 \pm 0.0510
	TripoSG	0.0129 \pm 0.0029	0.0246 \pm 0.0058	0.0480 \pm 0.0110	0.3794 \pm 0.0836	0.3791 \pm 0.0775
	SAM3D	0.0115 \pm 0.0041	0.0233 \pm 0.0080	0.0453 \pm 0.0151	0.4043 \pm 0.0590	0.3973 \pm 0.0583
BTCV	Hunyuan3D-2.1	0.0219 \pm 0.0244	0.0321 \pm 0.0284	0.0608 \pm 0.0509	0.4974 \pm 0.3187	0.4558 \pm 0.2234
	Direct3D	0.0470 \pm 0.0502	0.0572 \pm 0.0582	0.1032 \pm 0.0923	0.3202 \pm 0.1307	0.3370 \pm 0.1216
	Hi3DGen	0.0333 \pm 0.0230	0.0580 \pm 0.0313	0.1081 \pm 0.0544	0.3331 \pm 0.1674	0.3418 \pm 0.1275
	TripoSG	0.0420 \pm 0.0474	0.0515 \pm 0.0530	0.0936 \pm 0.0863	0.3523 \pm 0.1746	0.3688 \pm 0.1428
	SAM3D	0.0280 \pm 0.0207	0.0510 \pm 0.0262	0.0959 \pm 0.0464	0.3005 \pm 0.1088	0.3113 \pm 0.0852
MSD Lung	Hunyuan3D-2.1	0.0132 \pm 0.0229	0.0191 \pm 0.0235	0.0365 \pm 0.0419	0.5904 \pm 0.2133	0.5613 \pm 0.1889
	Direct3D	0.0131 \pm 0.0105	0.0153 \pm 0.0124	0.0299 \pm 0.0235	0.5865 \pm 0.1337	0.5609 \pm 0.1163
	Hi3DGen	0.0175 \pm 0.0118	0.0385 \pm 0.0198	0.0735 \pm 0.0358	0.4047 \pm 0.1276	0.3843 \pm 0.1086
	TripoSG	0.0115 \pm 0.0176	0.0140 \pm 0.0206	0.0268 \pm 0.0370	0.6216 \pm 0.1705	0.6074 \pm 0.1239
	SAM3D	0.0166 \pm 0.0094	0.0381 \pm 0.0172	0.0729 \pm 0.0312	0.3656 \pm 0.1020	0.3478 \pm 0.0815
MSD Brain	Hunyuan3D-2.1	0.0114 \pm 0.0124	0.0190 \pm 0.0178	0.0367 \pm 0.0331	0.5449 \pm 0.2394	0.5397 \pm 0.2148
	Direct3D	0.0158 \pm 0.0099	0.0234 \pm 0.0152	0.0453 \pm 0.0285	0.4212 \pm 0.1460	0.4363 \pm 0.1318
	Hi3DGen	0.0189 \pm 0.0108	0.0391 \pm 0.0173	0.0747 \pm 0.0314	0.3811 \pm 0.1351	0.3856 \pm 0.1206
	TripoSG	0.0121 \pm 0.0096	0.0187 \pm 0.0185	0.0361 \pm 0.0347	0.4583 \pm 0.1418	0.4756 \pm 0.1290
	SAM3D	0.0147 \pm 0.0059	0.0338 \pm 0.0134	0.0650 \pm 0.0249	0.3190 \pm 0.0757	0.3290 \pm 0.0735
MSD Liver	Hunyuan3D-2.1	0.0219 \pm 0.0186	0.0335 \pm 0.0224	0.0640 \pm 0.0414	0.4641 \pm 0.2283	0.4581 \pm 0.1987
	Direct3D	0.0241 \pm 0.0210	0.0386 \pm 0.0248	0.0732 \pm 0.0451	0.4545 \pm 0.2341	0.4405 \pm 0.1887
	Hi3DGen	0.0247 \pm 0.0163	0.0470 \pm 0.0272	0.0885 \pm 0.0482	0.3939 \pm 0.2226	0.3887 \pm 0.1835
	TripoSG	0.0251 \pm 0.0195	0.0379 \pm 0.0249	0.0720 \pm 0.0449	0.4030 \pm 0.1859	0.4029 \pm 0.1512
	SAM3D	0.0262 \pm 0.0115	0.0485 \pm 0.0237	0.0917 \pm 0.0429	0.3273 \pm 0.0987	0.3436 \pm 0.1064
Duke Cspine	Hunyuan3D-2.1	0.0718 \pm 0.0535	0.0915 \pm 0.0668	0.1610 \pm 0.1092	0.3017 \pm 0.2908	0.2982 \pm 0.2054
	Direct3D	0.0956 \pm 0.0595	0.1276 \pm 0.0814	0.2173 \pm 0.1236	0.2183 \pm 0.2254	0.2347 \pm 0.1639
	Hi3DGen	0.0894 \pm 0.0676	0.1344 \pm 0.1018	0.2231 \pm 0.1551	0.3162 \pm 0.3945	0.2956 \pm 0.2698
	TripoSG	0.0596 \pm 0.0442	0.0718 \pm 0.0566	0.1290 \pm 0.0940	0.3828 \pm 0.3606	0.3445 \pm 0.2306
	SAM3D	0.0959 \pm 0.0478	0.1230 \pm 0.0648	0.2134 \pm 0.0981	0.1276 \pm 0.1075	0.1568 \pm 0.0887
GSO	Hunyuan3D-2.1	0.0286 \pm 0.0482	0.0596 \pm 0.0730	0.1052 \pm 0.1065	0.3980 \pm 0.1809	0.3542 \pm 0.1292
	Direct3D	0.0290 \pm 0.0392	0.0609 \pm 0.0660	0.1088 \pm 0.0976	0.3800 \pm 0.1720	0.3409 \pm 0.1226
	Hi3DGen	0.0258 \pm 0.0332	0.0600 \pm 0.0670	0.1070 \pm 0.0994	0.3868 \pm 0.1752	0.3516 \pm 0.1243
	TripoSG	0.0302 \pm 0.0539	0.0630 \pm 0.0763	0.1109 \pm 0.1068	0.3765 \pm 0.1735	0.3401 \pm 0.1233
	SAM3D	0.0683 \pm 0.0580	0.1814 \pm 0.1363	0.2867 \pm 0.1853	0.1547 \pm 0.1783	0.1700 \pm 0.1322
Animal3D	Hunyuan3D-2.1	0.0216 \pm 0.0096	0.0435 \pm 0.0171	0.0829 \pm 0.0313	0.3601 \pm 0.1329	0.3281 \pm 0.1067
	Direct3D	0.0186 \pm 0.0094	0.0400 \pm 0.0165	0.0764 \pm 0.0297	0.3834 \pm 0.0995	0.3649 \pm 0.0779
	Hi3DGen	0.0286 \pm 0.0160	0.0605 \pm 0.0288	0.1128 \pm 0.0497	0.3134 \pm 0.1147	0.3117 \pm 0.0905
	TripoSG	0.0335 \pm 0.0169	0.0644 \pm 0.0291	0.1196 \pm 0.0504	0.2788 \pm 0.0983	0.2861 \pm 0.0873
	SAM3D	0.0243 \pm 0.0111	0.0486 \pm 0.0180	0.0921 \pm 0.0320	0.3717 \pm 0.0940	0.3740 \pm 0.0723

Table A1: Benchmark performance across datasets

References

- [1] Kawamura, R. *et al.* Feasibility of left ventricular volume measurements by three-dimensional speckle tracking echocardiography depends on image quality and degree of left ventricular enlargement: Validation study with cardiac magnetic resonance imaging. *Journal of Cardiology* **63**, 230–238 (2014).
- [2] Zackrisson, S. *et al.* One-view breast tomosynthesis versus two-view mammography in the malmö breast tomosynthesis screening trial (mbtst): a prospective, population-based, diagnostic accuracy study. *The Lancet Oncology* **19**, 1493–1503 (2018).
- [3] Dhamija, E., Gulati, M., Deo, S. V., Gogia, A. & Hari, S. Digital breast tomosynthesis: An overview. *Indian Journal of Surgical Oncology* **12**, 315–329 (2021).
- [4] Gefter, W. B. & Hatabu, H. Reducing errors resulting from commonly missed chest radiography findings. *Chest* **163**, 634–649 (2023).
- [5] Foti, G. & Longo, C. Deep learning and ai in reducing magnetic resonance imaging scanning time: Advantages and pitfalls in clinical practice. *Polish Journal of Radiology* **89**, 443–451 (2024).
- [6] GharehMohammadi, F. & Sebro, R. A. Efficient health care: Decreasing mri scan time. *Radiology: Artificial Intelligence* **6** (2024).
- [7] Ying, X. *et al.* X2ct-gan: Reconstructing ct from biplanar x-rays with generative adversarial networks (2019). [arXiv:1905.06902](https://arxiv.org/abs/1905.06902).
- [8] Bourigault, E., Hamdi, A. & Jamaludin, A. X-diffusion: Generating detailed 3d mri volumes from a single image using cross-sectional diffusion models (2025). [arXiv:2404.19604](https://arxiv.org/abs/2404.19604).
- [9] Hunyuan3D, T. *et al.* Hunyuan3d 2.1: From images to high-fidelity 3d assets with production-ready pbr material (2025). URL <https://arxiv.org/abs/2506.15442>. [arXiv:2506.15442](https://arxiv.org/abs/2506.15442).
- [10] Wu, S. *et al.* Direct3d: Scalable image-to-3d generation via 3d latent diffusion transformer (2024). URL <https://arxiv.org/abs/2405.14832>. [arXiv:2405.14832](https://arxiv.org/abs/2405.14832).
- [11] Li, Y. *et al.* Tripogs: High-fidelity 3d shape synthesis using large-scale rectified flow models (2025). URL <https://arxiv.org/abs/2502.06608>. [arXiv:2502.06608](https://arxiv.org/abs/2502.06608).
- [12] Ye, C. *et al.* Hi3dgen: High-fidelity 3d geometry generation from images via normal bridging (2025). URL <https://arxiv.org/abs/2503.22236>. [arXiv:2503.22236](https://arxiv.org/abs/2503.22236).
- [13] Team, S. D. *et al.* Sam 3d: 3dfy anything in images (2025). URL <https://arxiv.org/abs/2511.16624>.

- [14] Støverud, K.-H. *et al.* Aeropath: An airway segmentation benchmark dataset with challenging pathology (2023). URL <https://arxiv.org/abs/2311.01138>. [arXiv:2311.01138](https://arxiv.org/abs/2311.01138).
- [15] Landman, B. A. *et al.* Multi-atlas labeling beyond the cranial vault – workshop and challenge. Synapse (Project: syn3193805) (2015). URL <https://www.synapse.org/Synapse:syn3193805>.
- [16] Zhou, L., Wiggins, W., Zhang, J. *et al.* The duke university cervical spine mri segmentation dataset (cspineseg). *Scientific Data* **12**, 1695 (2025). URL <https://doi.org/10.1038/s41597-025-05975-w>.
- [17] Antonelli, M. *et al.* The medical segmentation decathlon. *Nature Communications* **13**, 4128 (2022). URL <https://www.nature.com/articles/s41467-022-30695-9>.
- [18] Xu, J. *et al.* Animal3d: A comprehensive dataset of 3d animal pose and shape 9065–9075 (2023).
- [19] Downs, L. *et al.* Google scanned objects: A high-quality dataset of 3d scanned household items (2022).